RESEARCH PAPER

Sol-gel Approach for the Synthesis and Characterization of Mg and Cu Substituted Mn-Zn Ferrite Nanoparticles

Amit Bandekar[1,*], Pravin Tirmali[2], Paresh Gaikar[3], Shriniwas Kulkarni[4], Nana Pradhan[1]

* *amitbandekar78@gmail.com*

[1] Department of Physics, Ramnarain Ruia Autonomous College, Mumbai, Maharashtra, India
[2] Application Specialist, I.R. Technology Services Pvt. Ltd., Navi Mumbai Maharashtra, India
[3] Department of Physics, Rayat Shikshan Sanstha's, Karmaveer Bhaurao Patil College, Vashi, Maharashtra, India
[4] Department of Physics, The Institute of Science, Mumbai, Maharashtra, India

Received: December 2023 **Revised: March 2024** **Accepted: March 2024**
DOI: 10.22068/ijmse.3542

Abstract: *The Mn-Zn ferrite with a composition of $Mn_{0.25}Mg_{0.08}Cu_{0.25}Zn_{0.42}Fe_2O_4$ has been synthesized in this study using the chemical sol-gel technique at a pH of 7. The sample was prepared and subsequently annealed at a temperature of 700°C. The nanocrystalline ferrite samples were subjected to characterization using X-ray diffraction (XRD), Fourier transform-infrared spectroscopy (FT-IR), Scanning electron microscopy (SEM), Thermogravimetry (TG), and Differential thermal analysis (DTA). The findings of these observations are delineated and deliberated. The sample's phase composition was verified using X-ray diffraction examination. The crystalline size was determined using Scherrer's formula and was observed to be within the range of 20-75 nm. Two notable stretching bands were seen in the FTIR spectra within the range of 400-650 cm^{-1}. The spinel structure of the produced nanoparticles was confirmed by these two bands. The magnetic characteristics of the powder were examined using a Vibrating Sample Magnetometer (VSM). The presence of M-H hysteresis loops suggests that the produced nanoparticles have superparamagnetic properties, as evidenced by their low coercive force, remanent magnetization, and saturation magnetization values.*

Keywords: *Ferrite, Sol-gel method, XRD, FT-IR, TG-DTA, VSM, Nanocrystalline, Superparamagnetic.*

1. INTRODUCTION

To carry out scientific and industrial applications and keep up with cutting-edge technological advances, nanoparticles are among the most dependable and outstanding supplies. Nanoparticles from the ferrite group are one of the many important nanoparticle classes helping to advance manufacturing across the globe. Due to its excellent soft magnetic properties and good performance-cost ratio, Mn-Zn ferrites are widely employed in domestic appliances, communication, computers, and other electronic industries [1-2]. Because of their high initial magnetic permeability, saturation magnetization, electrical resistivity, and low power losses [3], Mn-Zn ferrites are among the most important soft magnetic materials. Due to the trend toward lightweight, downsizing, and multifunction in electronic equipment, high permeability and low loss in Mn-Zn ferrites are becoming increasingly important qualities. In a unit cell of Mn-Zn ferrite, there are 64 tetrahedral sites (A-site) and 32 octahedral sites (B-site), as is typical of spinel structures. The unit cell contained 72 empty spots due to the metal cations filling just 8 A-sites and 16 B-sites. Magnetic divalent cations, like Mn^{2+}, typically favour octahedral sites and create an anti-spinel structure. In this crystal structure, rare earth ions, among other metallic ions, can be introduced into the lattice to alter its structure and magnetic properties [5, 6].

Chemical doping has been widely used in developing ferrites in recent years. The microstructure and characteristics of Mn-Zn ferrites can be varied by adding one of three types of additions. The microstructure and inherent characteristics of ferrites can be altered by introducing additives such as CuO, MgO, and CoO into the spinel lattice [7-8]. Traditional additives have been investigated extensively for their impact on Mn-Zn ferrite's magnetic characteristics. There are several techniques for obtaining magnetic ferrite particles, but some of them have significant limitations that limit the potential for future development in the performance of the produced materials [9, 10]. To address these limitations and satisfy the needs of emerging industries, researchers have developed several wet chemical processes like sol-gel citrate solution [11, 12], hydrothermal method [13], micro-emulsion process [14], co-sedimentation

[DOI: 10.22068/ijmse.3542]

technique [15], and solution atomization [16], also known as emulsion blasting. Sol-gel synthesis is one of the many chemical processes accessible; it allows for the creation of nanoparticles, hence spawning a new category of unique materials. The chemical composition and crystal structure of these materials are similar to those of their alloys generated using conventional techniques such as solid-state reaction pathways, but their shape is distinct and improved because of their small particle size. Crystallization in the colloidal state may now be developed at low temperatures (100°C) thanks to recent discoveries in sol-gel technology. This paved the way for the development of the low-temperature sol-gel technique for the synthesis of nanocrystalline oxides, mixed oxides, and composite materials [17]. Nevertheless, a complete understanding of how the soft magnetic properties of Mn-Zn ferrites are influenced by divalent ion modification remains elusive. As raw materials, we utilize nitrates of AR grade, ammonia, and citric acid to produce Mg and Cu substituted Mn-Zn ferrite ($Mn_{0.25}Mg_{0.08}Cu_{0.25}Zn_{0.42}Fe_2O_4$) using chemical sol-gel. The impact of doping Mn-Zn ferrite with divalent ions on its structure and magnetic properties has been investigated.

2. EXPERIMENTAL PROCEURES

2.1. Synthesis of $Mn_{0.25}Mg_{0.08}Cu_{0.25}Zn_{0.42}Fe_2O_4$ Nanoparticle

Due to their ease of solubility in water, the starting materials for the sol-gel method, also known as sol-gel auto combustion, sol-gel autoignition, or sol-gel self-combustion, are the nitrates of the constituent metal ions and a suitable chelating agent (fuel), such as urea/glycine/citric acid. In most cases, a ratio of 1:x (where x can range from 1 to 3) of metal nitrate to citrate is used. In the vast majority of instances, the reaction process is carried out in the open air, unprotected by inert gases. The flowchart of the sol-gel method is shown in Fig. 1. Metal nitrates should be dissolved in double-distilled or deionized water in sufficient quantity (say 100 ml for 1 gram of metal nitrates) to produce a transparent solution. Citric acid in water must be combined with metal nitrates solution, which must be heated to 90 degrees Celsius while being stirred constantly. The pH was kept at 7 with the use of ammonia. In most cases, the fluid thickened into a gel of a brownish-green color. A little bit of gel was set away for thermogravimetric analysis and differential thermal analysis. After all of the water molecules evaporated, the heated gel became foamy. Later on, the gel spontaneously caught fire and burned with flaming flints that reached extremely high temperatures. The citrate complex is consumed in its entirety while the ignition and breakdown process continues. In only a few short minutes, the auto-ignition process can be finished, leaving behind the brown ashes of a forerunner. The samples were then sintered at 700°C for 2 hours before being cooled gently in the muffle furnace.

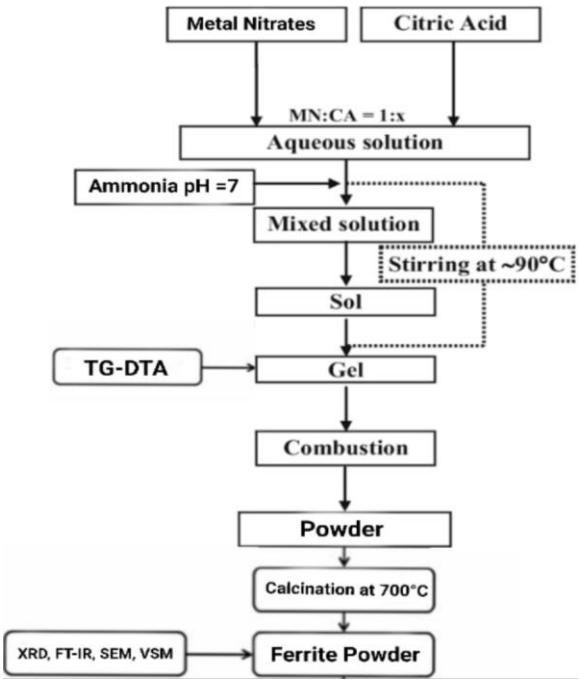

Fig. 1. Flowchart of the sol-gel auto combustion method.

2.2. Characterization

The Rigaku Miniflex 600 X-ray diffractometer was used to determine the phase composition of the samples using Cu-K radiation (λ= 0.154056nm). The materials' microstructure was examined with an FE-SEM, ZEISS Ultra60 scanning electron microscope. Hitachi STA7300 was used to conduct TG and DTA characterization tests up to 1000°C at a rate of 20°C/min. Using a Shimadzu IR Prestige-21 FT-IR spectrometer, infrared spectra were acquired for the produced sample across the range of 400 to 4000 cm^{-1}. The Lakeshore VSM was used to analyze the magnetic characteristics, such as the M-H curve, at temperatures of 15 K and 300

[DOI: 10.22068/ijmse.3542]

K in a magnetizing field of 2T.

3. RESULTS AND DISCUSSION

3.1. X-ray Diffraction

When it comes to the characterization of crystalline materials, X-ray diffraction (XRD) is one of the most essential methods that may be used. By analyzing the XRD pattern of a material, one may acquire information about the many crystallographic phases that are present, as well as the parameters of the unit cell and the presence or absence of impurities, among other things. The analysis of the samples was conducted using particle size X-ray diffraction spectroscopy with Cu-K radiation (λ= 1.5406 Å) at room temperature. It was determined that the samples showed a structure consistent with cubic spinel particles. This finding prompted a discussion on the structural and magnetic properties of ferrite manganese zinc. The observed peaks resulting from the particle tests were subsequently compared to the expected peaks and standards.

The Debye-Scherrer equation 1 was also used to determine the crystalline sizes. [18-19]. The average crystalline size of the sintered $Mn_{0.25}Mg_{0.08}Cu_{0.25}Zn_{0.42}Fe_2O_4$ ferrite sample was 47.04 nm. Table 2 shows the value of average crystalline size (D), interplanar spacing (d_{hkl}) and packing factor (P). Average crystalline size (D), interplanar spacing (d_{hkl}) and lattice constant were calculated by using Braggs equations. Interplanar spacing (d), packing factor (P) and Lattice constant (a) have been determined using equations 2, 3, and 4 respectively

$$D= K\lambda/\beta\cos\theta \quad (1)$$

$$d= 2d\sin\theta/n\lambda \quad (2)$$

$$P= D/d \quad (3)$$

$$a= d(h^2+k^2+l^2)^{½} \quad (4)$$

Where D= Crystalline size, K= Debye Scherer constant (0.9), a= lattice constant, λ= Wavelength of light (1.5406 Å for Kα), β= Full-width at half maximum of the peaks and θ= Diffraction angle, p= Packing fraction, d= Interplanar spacing, n= Order of the reflection and h, k, l are the miller indices of cubic structure. The values of lattice parameters, crystallite size, interplanar spacing and packing factor have been given in Table 1 and Table 2.

The XRD pattern of the Mn-Zn ferrite doped with Mg and Cu ($Mn_{0.25}Mg_{0.08}Cu_{0.25}Zn_{0.42}Fe_2O_4$) is shown in Fig. 2.

Table 1. Values of lattice parameters.

Phase name	a Å	b Å	c Å	α ⁰	β ⁰	γ ⁰
MZF	8.42123	8.42123	8.42123	90.00	90.00	90.00
Hematite	5.04103	5.04103	13.75753	90.00	90.00	120.00
Cuprospinel	8.33934	8.33934	8.33934	90.00	90.00	90.00
Copper manganese iron oxide	8.42099	8.42099	8.42099	90.00	90.00	90.00
Magnesioferrite	8.42119	8.42119	8.42119	90.00	90.00	90.00

Table 2. Crystallite size, Interplanar spacing and Packing factor.

Sample	D nm	d nm	P
$Mn_{0.25}$ $Mg_{0.08}$ $Cu_{0.25}$ $Zn_{0.42}$ Fe_2O_4	47.04	0.19708	238.68

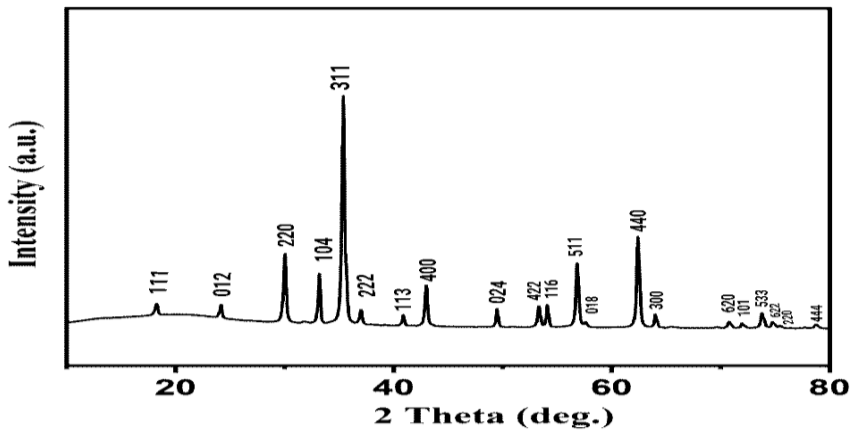

Fig. 2. XRD graph of sample $Mn_{0.25}$ $Mg_{0.08}$ $Cu_{0.25}$ $Zn_{0.42}$ Fe_2O_4

[DOI: 10.22068/ijmse.3542]

The patterns are catalogued using the accepted method of XRD pattern indexing. The peaks and their matching crystallographic planes are shown graphically in X-ray diffraction studies. XRD data analysis and improvement were performed using Smartlab Studio II software. JCPDS-ICDD database card numbers 00-069-0164 (MZF), 01-071-5088 (Hematite), 00-025-0283 (Cuprospinel), 01-082-2852 (Copper manganese iron oxide), and 01-076-2875 (Magnesioferrite) are used to match indexed peaks from S/M: PDF2, 2023.

3.2. FTIR Analysis

Sample $Mn_{0.25}Mg_{0.08}Cu_{0.25}Zn_{0.42}Fe_2O_4$ FTIR spectra collected in the 4000-400 cm^{-1} range are displayed in Fig. 3. Tetrahedral complexes are thought to be responsible for the absorption band (υ_1) around 630 cm^{-1}, whereas octahedral complexes are thought to be responsible for band (υ_2) about 530 cm^{-1} [20–21].

Table 3 lists the tetrahedral and octahedral vibration frequencies. The hydroxyl group and the bands around 1577 cm^{-1} and 1450 cm^{-1} C=O stretching vibration peak are responsible for the bandwidth surrounding O-H stretching vibration peaks 3354 cm^{-1} and 3284 cm^{-1}. The band with the highest wavenumber was detected at approximately 630 cm^{-1}, which is indicative of the metal's intrinsic stretching vibration at the tetrahedral location. The synthesis of $Mn_{0.25}Mg_{0.08}Cu_{0.25}Zn_{0.42}Fe_2O_4$ is confirmed by the band around 530 cm^{-1}, which is due to octahedral metal stretching. The band around 1000 cm^{-1} is associated with the peak of the C-O stretching vibration.

The FTIR spectrum was carefully analyzed, and each of the prominent peaks was investigated, confirming the presence of the ferrite phase.

3.3. 3.3 Thermal Analysis

Using TG-DTA, the thermal stability of $Mn_{0.25}Mg_{0.08}Cu_{0.25}Zn_{0.42}Fe_2O_4$ nanomaterials was examined from room temperature to 1000°C at a rate of 20°C per minute. The relative weight variation as the samples were heated in the air is displayed in Fig. 4, which shows that the initial 19% weight loss is linked to an endothermic peak and is related to water loss, which happens in two stages: first, dehydration, and later, loss of adsorbed water till 205°C [22]. The second weight loss 59.55% is attributed to a significant exothermic peak suggesting decarbonization of the materials [22-23].

Up to 275°C, the decarbonization process continued (Fig. 4). The third weight loss of 5.84% from a temperature range of 275°C to 500°C and the fourth weight loss of 5.84% from a temperature range of 500°C to 650°C may be associated with the combustion of nitrates and remaining organic substances. Samples have developed an ordered condition, which makes them thermally stable at 650°C. Due to the growth of the crystalline phase, the generated nanomaterials in Figure 5 show differential thermal analysis (DTA) display exothermic peaks at roughly 220°C.

The low exothermic peak seen at 590°C may be explained by the rearranging of the crystal lattice. High-quality sample features can be seen in the TGA and DTA curves.

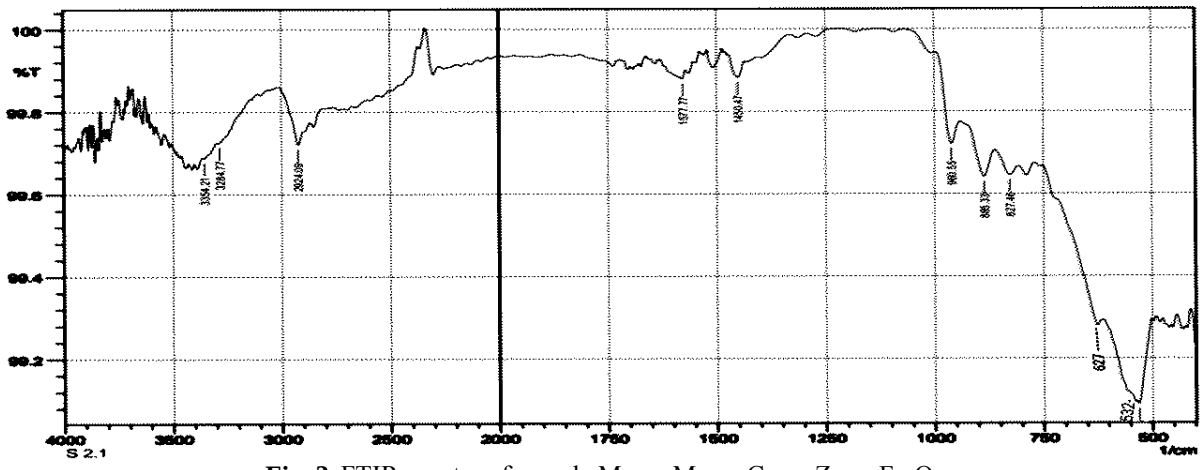

Fig. 3. FTIR spectra of sample $Mn_{0.25}$ $Mg_{0.08}$ $Cu_{0.25}$ $Zn_{0.42}$ Fe_2O_4

[DOI: 10.22068/ijmse.3542]

Table 3. Tetrahedral, octahedral vibration frequencies ν_1 and ν_2

Sample	υ_1 cm^{-1}	υ_2 cm^{-1}
$Mn_{0.25}$ $Mg_{0.08}$ $Cu_{0.25}$ $Zn_{0.42}$ Fe_2O_4	627	532

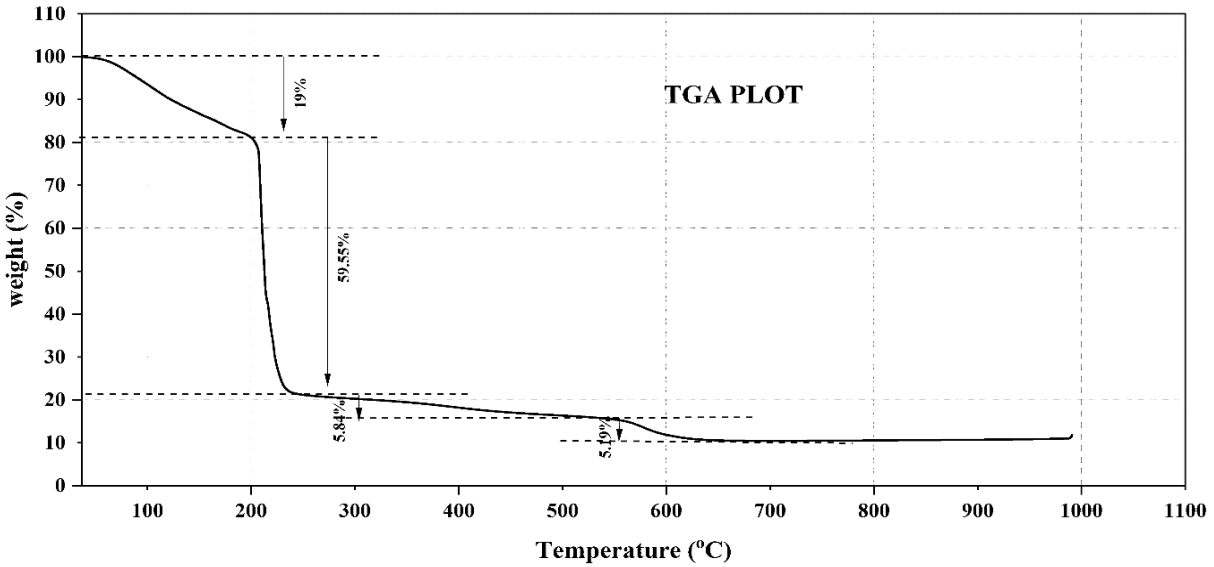

Fig. 4. TGA analysis of sample $Mn_{0.25}$ $Mg_{0.08}$ $Cu_{0.25}$ $Zn_{0.42}$ Fe_2O_4

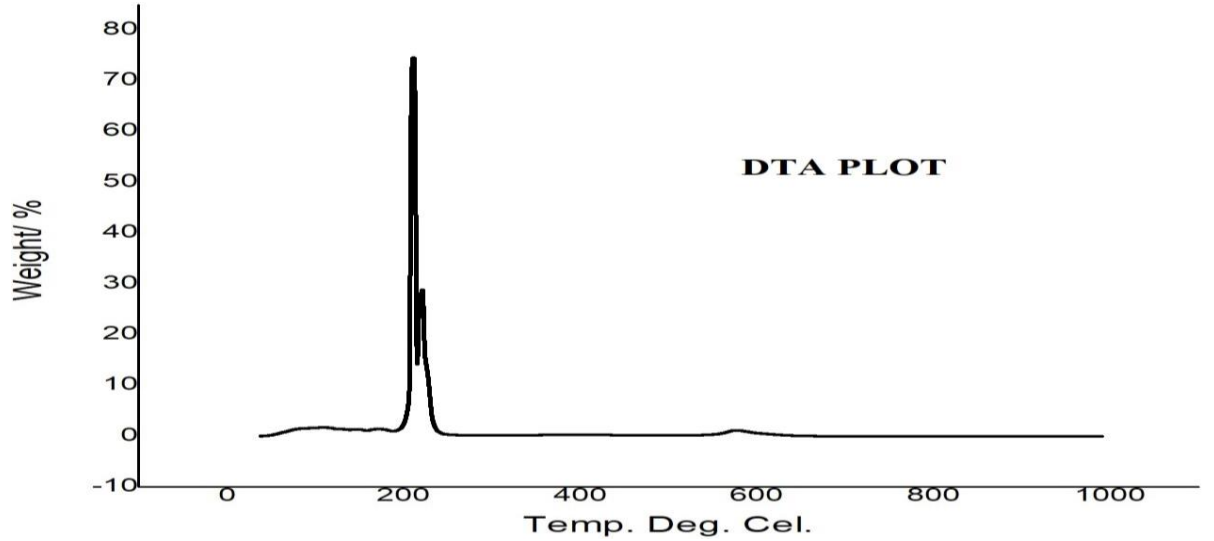

Fig. 5. DTA analysis of sample $Mn_{0.25}$ $Mg_{0.08}$ $Cu_{0.25}$ $Zn_{0.42}$ Fe_2O_4

3.4 SEM and EDX analysis

The morphological properties of $Mn_{0.25}$ $Mg_{0.08}$ $Cu_{0.25}$ $Zn_{0.42}$ Fe_2O_4 nanoparticles annealed at 700°C are displayed in Fig. 6 using the standard SEM examination. Small crystallites of different sizes and shapes can be observed developing into multigrain agglomerations. According to SEM scans, ferrite powders showed a uniform average grain size of around 4 μm, a coarse structure, and a crystalline microstructure. This illustrates that a higher number of nanocrystals assemble to form each grain when compared to the estimated nanocrystal size from the XRD results. The sample particles exhibit a range of sizes and shapes, and grain cohesion is attributed to magnetic attraction. The stoichiometric proportion of $Mn_{0.25}$ $Mg_{0.08}$ $Cu_{0.25}$ $Zn_{0.42}$ Fe_2O_4 nanoparticles annealed at 700°C is confirmed by EDX analysis, and Fig. 7 displays the percentage proportion of the constituent elements. The percentage of elemental weight is displayed in the weight and atomic percentage proportion tables; the constituent elemental proportion and ratios match the anticipated elemental proportion, with

[DOI: 10.22068/ijmse.3542]

iron (Fe) and oxygen (O) having the highest peaks across all samples [24]. A standard EDX examination shows that elements of Mn, Mg, Zn, Cu, Fe, and O are present in Fig. 7.

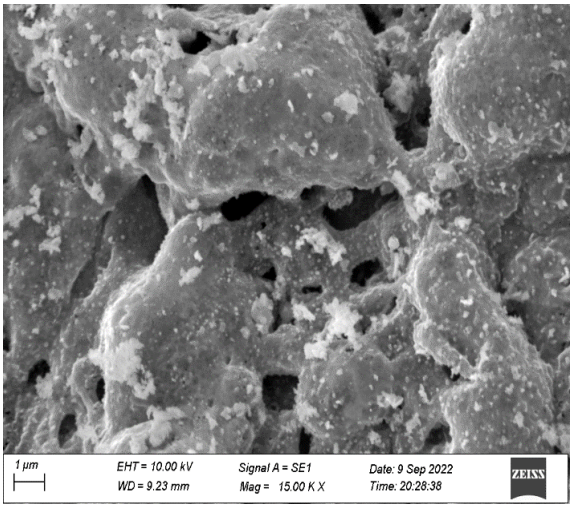

Fig. 6. SEM image of sample $Mn_{0.25}Mg_{0.08}Cu_{0.25}Zn_{0.42}Fe_2O_4$

3.4. Magnetic Properties

The VSM device was used to study the magnetic characteristics of the manufactured samples, which showed that the sample possesses paramagnetic properties through the tight hysteresis loop and that the magnetic field value for a sample at 15 K and 300 K temperatures. The relationship between M-H for $Mn_{0.25}Mg_{0.08}Cu_{0.25}Zn_{0.42}Fe_2O_4$ particles, reached ± 20 kOe at 15 K and ± 20 kOe at 300 K temperature. The magnetization (M) of the synthesized ferrite particles at 15 K and 300 K in the range of -4 to +4 kOe is plotted against a magnetic field (H) in Figure 8. With coercivity H_c= 108 Oe and saturation magnetization; M_s= 77 emu/g at 15 K temperature and coercivity H_c= 56.99 Oe and saturation magnetization; M_s= 41.75 emu/g at 300 K temperature, the synthesized sample exhibits soft magnet behavior. Table 4 shows the retentivity values for the magnetic nanocrystallites, which are M_r= 14.73 emu/g at 15 K and M_r= 8.06 emu/g at 300 K. The S= M_r/M_s remanence ratio of material $Mn_{0.25}Mg_{0.08}Cu_{0.25}Zn_{0.42}Fe_2O_4$is 0.19. The production technique, domain structure, crystal size, and anisotropy of the crystal all affect the magnetic characteristics of ferrite particles [25].

According to reports, particles with S< 0.5 interact through magnetostatic forces, whereas randomly oriented noninteracting particles that rotate coherently have S= 0.5 [26–27]. Consequently, in this study, particles engaging by magnetostatic interactions are given S values less than 0.5.

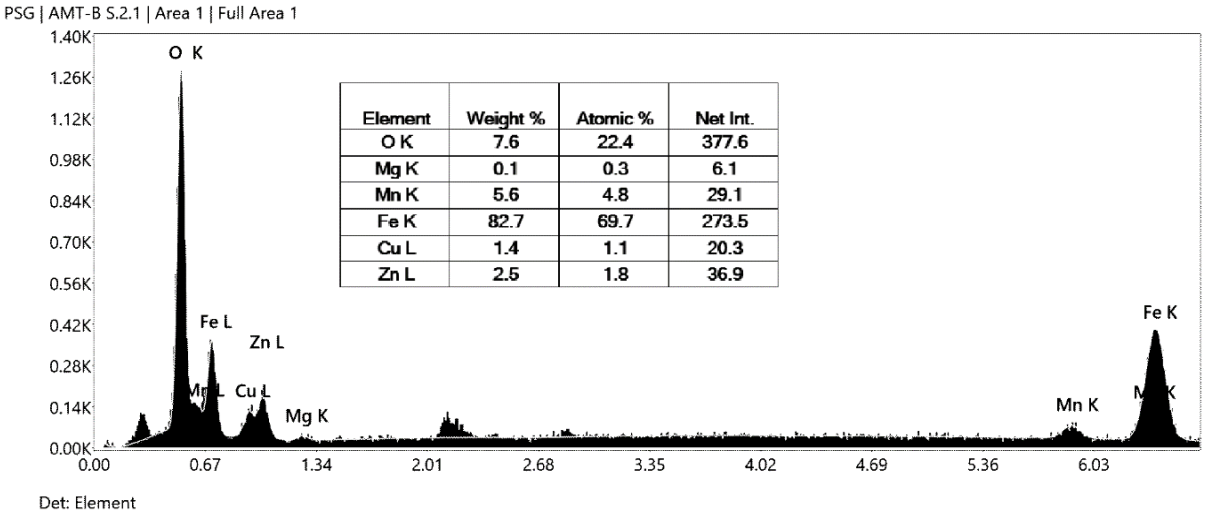

Element	Weight %	Atomic %	Net Int.
O K	7.6	22.4	377.6
Mg K	0.1	0.3	6.1
Mn K	5.6	4.8	29.1
Fe K	82.7	69.7	273.5
Cu L	1.4	1.1	20.3
Zn L	2.5	1.8	36.9

Fig. 7. EDX analysis of sample $Mn_{0.25}$ $Mg_{0.08}$ $Cu_{0.25}$ $Zn_{0.42}$ Fe_2O_4

Table 4. VSM calculated results of H_c, M_S, M_r & S.

Sample	Coercivity (H_c) (Oe)	Remanent Magnetization (M_r), (emu)/g	Saturation Magnetization (M_S) (emu)/g	S=M_r/M_S
$Mn_{0.25}$ $Mg_{0.08}$ $Cu_{0.25}$ $Zn_{0.42}$ Fe_2O_4 at 15 K	108	14.73	77	0.19
$Mn_{0.25}$ $Mg_{0.08}$ $Cu_{0.25}$ $Zn_{0.42}$ Fe_2O_4 at 300 K	56.99	8.06	41.75	0.19

[DOI: 10.22068/ijmse.3542]

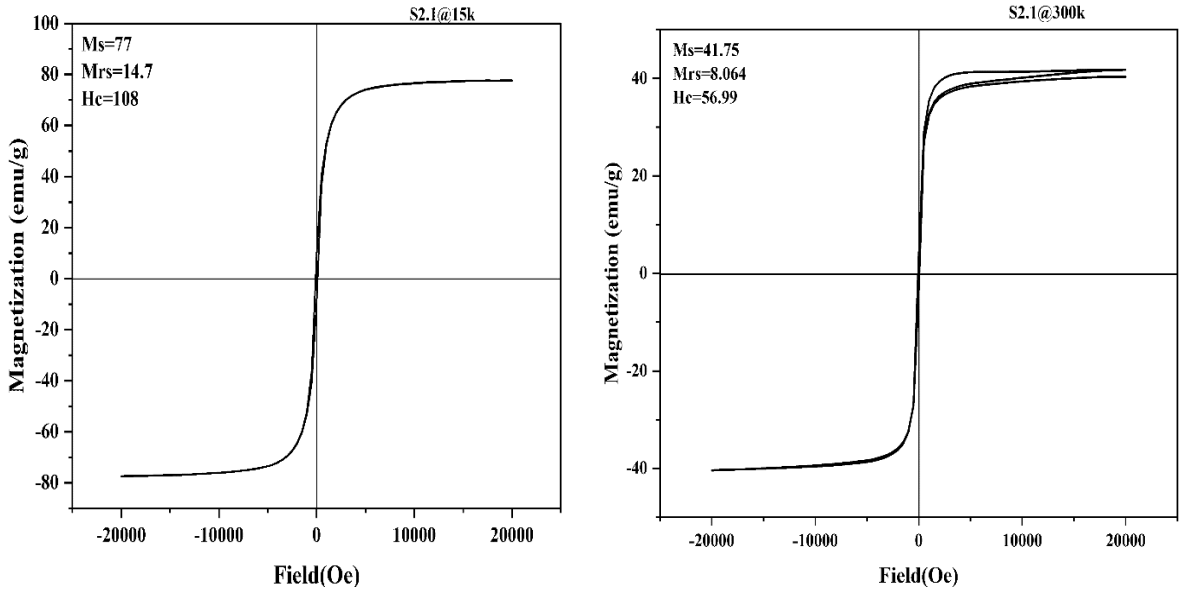

Fig. 8. M-H graph of sample $Mn_{0.25}$ $Mg_{0.08}$ $Cu_{0.25}$ $Zn_{0.42}$ Fe_2O_4 at 15 K and 300 K.

4. CONCLUSIONS

Nanoparticles of Mn-Zn ferrite with Mg and Cu substitutions have been prepared using the chemical sol-gel process, and their structures were studied using XRD. The resulting composition was $Mn_{0.25}Mg_{0.08}Cu_{0.25}Zn_{0.42}Fe_2O_4$. The particles have a consistent crystalline size of 47.04 nm on average, making them monodisperse. The IR spectra of the generated compound reveal the crystalline structure and vibrational modes of the ions. Using IR spectroscopy, the tetrahedral and octahedral high- and low-frequency bands of the resulting ferrite were determined. Multigrain agglomerations of tiny crystallites with irregular forms and a size of 4 μm were seen during a structural analysis of the screened samples using FE-SEM and EDX images. The phase transition temperature and thermal stability were investigated across a broad temperature range using TGA and DTA curves. Low coercivity, retentivity, and saturation magnetization are features of synthesized nanoparticles.

REFERENCES

[1]. Arulmurugan, R., Jeyadevan, B., Vaidyanathan, G. and Sendhilnathan, S., "Effect of zinc substitution on Co-Zn and Mn-Zn ferrite nanoparticles prepared by co-precipitation," J. Magn. Magn. Mater., 2005, 288, 470-477.

[2]. Hu, P., Yang, H. B., Pan, D. A., Wang, H., Tian, J. J., Zhang, S. G., Wang, X. F. and Volinsky, A. A., "Heat treatment effects on microstructure and magnetic properties of Mn-Zn ferrite powders," J. Magn. Magn. Mater., 2010, 322, 173-177.

[3]. Rath, C., Anand, S., Sahu, K.K., Kulkarni, S.D., Date, S.K., and Mishra, N.C., "Dependence on action distribution of particle size, lattice parameter, and magnetic properties in nanosize Mn-Zn ferrite", J. Appl. Phys., 2002, 91, 2211-2215.

[4]. Jiang, K. Q., Li, K. K., Peng, C. H. and Zhu, Y., "Effect of multi-additives on the microstructure and magnetic properties of high permeability Mn-Zn ferrite," J. Alloys Compd., 2012, 541, 472-476.

[5]. Su, H., Zhang, H. W., Tang, X. L., Shi and Y., "Effects of tungsten trioxide addition and top-temperature sintering period on properties of high-permeability NiCuZn ferrite," J. Alloys Compd., 2009, 468, 290-294.

[6]. Modak, S., Ammar, M., Mazaleyrat, F., Das, S. and Chakrabarti, P. K., "XRD, HRTEM and magnetic properties of mixed spinel nanocrystalline Ni-Zn-Cu-ferrite," J. Alloys Compd., 2009, 473, 15-19.

[7]. Shaikh, P. A., Kambale, R. C., Rao, A. V., and Kolekar, Y. D., "Studies on structural and electrical properties of $Co_{1-x}Ni_xFe_{1.9}Mn_{0.1}O_4$ ferrite," J. Alloys

[DOI: 10.22068/ijmse.3542]

Compd., 2009, 482, 276-282.
[8]. Heiba, Z. K., Mohamed, M. B., Wahba, A. M., Arda, L., "Magnetic and structural properties of nanocrystalline Cobalt-substituted magnesium-manganese ferrite," J. Supercond. Nov. Magn., 2015, 28, 2517-2524.
[9]. Kim, D. H., Nikles, D. E., and Brazel, C. S., "Synthesis and Characterization of Multifunctional Chitosan- $MnFe_2O_4$ Nanoparticles for Magnetic Hyperthermia and Drug Delivery," Materials, 2010, 3, 4051-4065.
[10]. Yang, H., Zhang, C., Shi, X., Hu, H., Du, X., Fang, Y., Ma, Y., Wu, H., and Yang, S., "Water-soluble superparamagnetic manganese ferrite nanoparticles for magnetic resonance imaging," Biomaterials, 2010, 31, 3667-3673.
[11]. Chao, L., Bingsuo, Z., Adam, J. R., and Zhang, Z. J., "Reverse Micelle Synthesis and Characterization of Superparamagnetic $MnFe_2O_4$ Spinel Ferrite Nanocrystallites," The Journal of Physical Chemistry B, 2000, 104, 1141-1145.
[12]. Chao, L. and Zhang, Z. J., "Size-Dependent Superparamagnetic Properties of Mn Spinel Ferrite Nanoparticles Synthesized from Reverse Micelles", Chemistry of Materials, 2001, 13, 2092-2096.
[13]. Adam, J. R., Chao, L. and Zhang, Z. J., "Determination of Magnetic Anisotropy Distribution and Anisotropy Constant of Manganese Spinel Ferrite Nanoparticles," The Journal of Physical Chemistry B, 2001, 105, 7967- 7971.
[14]. Christy, R. V., Song, Z. Q. and Zhang, Z. J., "Effects of Interparticle Interactions upon the Magnetic Properties of $CoFe_2O_4$ and $MnFe_2O_4$ Nanocrystals," The Journal of Physical Chemistry B, 2004**,** 108, 18222-18227.
[15]. Christy, R. V., and Zhang, Z. J, "Effects of Surface Coordination Chemistry on the Magnetic Properties of $MnFe_2O_4$ Spinel Ferrite Nanoparticles," Journal of the American Chemical Society, 2003, 125, 9828- 9833.
[16]. Yang, A., Chinnasamy, C. N., Greneche, J. M., Chen, Y. J., Yoon, S. D., Hsu, K., Vittoria, C. and Harris, V. G., "Large tunability of Néel temperature in Mn ferrite nanoparticles linked to growth- rate-induced cation inversion," Appl. Phys. Lett., 2009**,** 94,113109.
[17]. Toksha, B. G., Shirsath, S. E., Mane, M. L., Patange, S. M., Jadhav, S. S. and Jadhav, K. M., "Autocombustion high-temperature synthesis, structural and magnetic properties of $CoCr_xFe_{2-x}O_4$ ($0 \leq x \leq 1.0$)," J Phys Chem C., 2011, 115, 20905–20912.
[18]. Umut, E., Coskun, M., Pineider, F., Berti, D. and Güngüne¸, H., "Nickel ferrite nanoparticles for simultaneous use in magnetic resonance imaging and magnetic fluid hyperthermia," Journal of Colloid and Interface Science, 2019, 550, 199-209.
[19]. Shatti, W. A., Mubarak, T.H., and Mahmood, O. A., "Preparation and Study of the Properties of $Co_{1-x}Zn_xFe_2O_4$ Using Co- Precipitation Method," Diyala Journal For Pure Science, 2021, 17, 68-76.
[20]. Gabal, M.A., Al Angari, Y. M. and Kadi, M. W., "Structural and magnetic properties of nanocrystalline $Ni_{1-x}Cu_xFe_2O_4$ prepared through oxalates precursors," Polyhedron., 2011, 30, 1185-1190.
[21]. Mandal, K., Mandal, S. P., Agudo, P. and Pal, M., "A study of nanocrystalline (Mn–Zn) ferrite in SiO_2 matrix," Appl. Surf. Sci., 2002, 182, 386-389.
[22]. Turquat, C., Leroux, C., Gloter, A., Serin, V. and Nihoul, G., "V-doped HfO_2: thermal stability and vanadium valence," I. J. Inorg. Mater., 2001, 3, 1025-1032.
[23]. Zhao, L., Zhang, H., Xing, Y., Song, S., Yu, S., Shi, W., Guo, X., Yang, J., Lei, Y., and Cao, F., "Studies on the Magnetism of Cobalt Ferrite Nanocrystals Synthesized by Hydrothermal Method," J. Solid State Chem., 2008, 181, 245-252.
[24]. Almessiere, M. A., Slimani, Y., Shirsath, S., Wudil, Y. S., Baykal, A., and Ercan, I., "Customized magnetic properties of $(Mn_{0.5}Zn_{0.5})[Eu_xNd_xFe_{2-2x}]O_4$ nano spinel ferrites synthesized via ultrasonic irradiation approach," Results in Physics., 2020, 19, 103350.
[25]. Qu, Y., Yang, H., Yang, N., Fan, Y., Zhu, H., and Zou, G., "The effect of reaction temperature on the particle size, structure and magnetic properties of coprecipitated

[DOI: 10.22068/ijmse.3542]

$CoFe_2O_4$ nanoparticles," Mater. Lett., 2006, 60, 3548-3552.

[26]. Wang, Z. L., Liu, Y. and Zhang, Z. Handbook of Nanophase and Nanostructured Materials, vol. II and III, Kluwer Academic, Springer, New York, 2003, 595-625.

[27]. Stoner, E. C. and Wohlfarth, E. P. "A mechanism of magnetic hysteresis in heterogeneous alloys," Philos. Trans. R. Soc. Lond., 1948, 240, 599.

[DOI: 10.22068/ijmse.3542]